Temperature Dependence of Coherent versus Spontaneous Raman Scattering

Giovanni Batignani,[1,2,*] Emanuele Mai,[1,2] Miles Martinati,[1] Mohanan M. Neethish,[1]
Shaul Mukamel,[3] and Tullio Scopigno[1,2,4,†]
[1]*Dipartimento di Fisica, Universitá di Roma "La Sapienza", Roma I-00185, Italy*
[2]*Center for Life Nano Science @Sapienza, Istituto Italiano di Tecnologia, Viale Regina Elena 291, I-00161 Roma, Italy*
[3]*Department of Chemistry, University of California, Irvine, California 92623, USA*
[4]*Istituto Italiano di Tecnologia, Graphene Labs, Via Morego 30, I-16163 Genova, Italy*

(Received 17 October 2023; revised 27 August 2024; accepted 7 October 2024; published 15 November 2024)

Because of their sub picosecond temporal resolution, coherent Raman spectroscopies have been proposed as a viable extension of spontaneous Raman thermometry, to determine dynamics of mode specific vibrational energy content during out of equilibrium molecular processes. Here we show that the presence of multiple laser fields stimulating the vibrational coherences introduces additional quantum pathways, resulting in destructive interference. This ultimately reduces the thermal sensitivity of single spectral lines, nullifying it for harmonic vibrations and temperature independent polarizability. We demonstrate how harnessing anharmonic signatures such as vibrational hot bands enables coherent Raman thermometry.

DOI: 10.1103/PhysRevLett.133.206902

Ever since the Raman effect was first discovered, the classical description of the scattering process has emphasized the temperature dependence of the Raman cross section, being activated through the polarizability modulations generated by the structural fluctuations with respect to the equilibrium state [1]. While this classical picture captures the essence of the physical process by predicting larger Raman signals at higher temperatures, it fails to provide a quantitative description of the measured responses. Indeed, it does not account for the temperature-dependent Stokes and anti-Stokes line intensities, nor does it predict a nonvanishing (Stokes) response as the temperature approaches absolute 0 K. This discrepancy can be attributed to the low occupation numbers typically associated with thermal excitations [2], revealing the quantum nature of vibrational levels. Temperature modifications can also alter the optical polarizability [3,4], for example, by inducing phase transitions, density changes or anisotropic fluctuations, ultimately affecting the intensity, position, and widths of the Raman lines [5–10]. Under low light excitation regimes [11], the ratio of Stokes (I_S) and anti-Stokes (I_{AS}) line intensities is linked to the temperature by the equation: $(I_S/I_{AS}) = (\nu_S^3/\nu_{AS}^3)e^{(\hbar\omega_0/k_BT)}$, with $\nu_S = \nu_R - \nu_0$ and $\nu_{AS} = \nu_R + \nu_0$ indicating the frequencies of Stokes and anti-Stokes emissions. This serves as a powerful noncontact tool for extracting the equilibrium temperature of the investigated sample, being routinely applied for the characterization of gas flames, liquids, solid state compounds [12,13], as well as for studying relaxation processes [14–16] and thermal transport [17,18].

Early observation of an asymmetry between the vibrational response in the red and in the blue side of the spectrum (corresponding to lower and higher frequency probe pulses relative to the pump) measured by stimulated Raman spectroscopy (SRS) experiments [19] has been interpreted in terms of Stokes and anti-Stokes temperature dependent ratio, in line with the spontaneous Raman (SR) scenario, advancing a straightforward application of SRS for thermometry [20]. Theoretical contributions [21] clarified that, in striking contrast with SR, the same (thermal) populations concur to the generation of red- and blueshifted SRS components, which hence cannot be compared to extract the temperature.

Here, we build on a diagrammatic framework to dissect the different processes that concur to the generation of nonlinear Raman responses [22,23], studying how the thermal distribution affects the measured signals. SRS accesses the vibrational spectrum, combining a narrowband Raman pump (RP) and broadband probe (PP) [24–26]: the interaction of the sample with PP spectral components shifted by one vibrational quantum with respect to the RP stimulates vibrational coherences, which in turn modulate the macroscopic polarizability, generating Raman bands on top of the probe spectrum [27,28]. Coherent Raman spectroscopy (CRS) is also exploited to probe vibrational excitations directly in the time-domain [29–32]: a femtosecond RP stimulates vibrational coherences, which are then recorded by scanning the time-dependent transmissivity via a broadband PP [33–36], a scheme known as impulsive stimulated Raman scattering (ISRS). Adding a

---

[*] Contact author: giovanni.batignani@uniroma1.it

[†] Contact author: tullio.scopigno@uniroma1.it

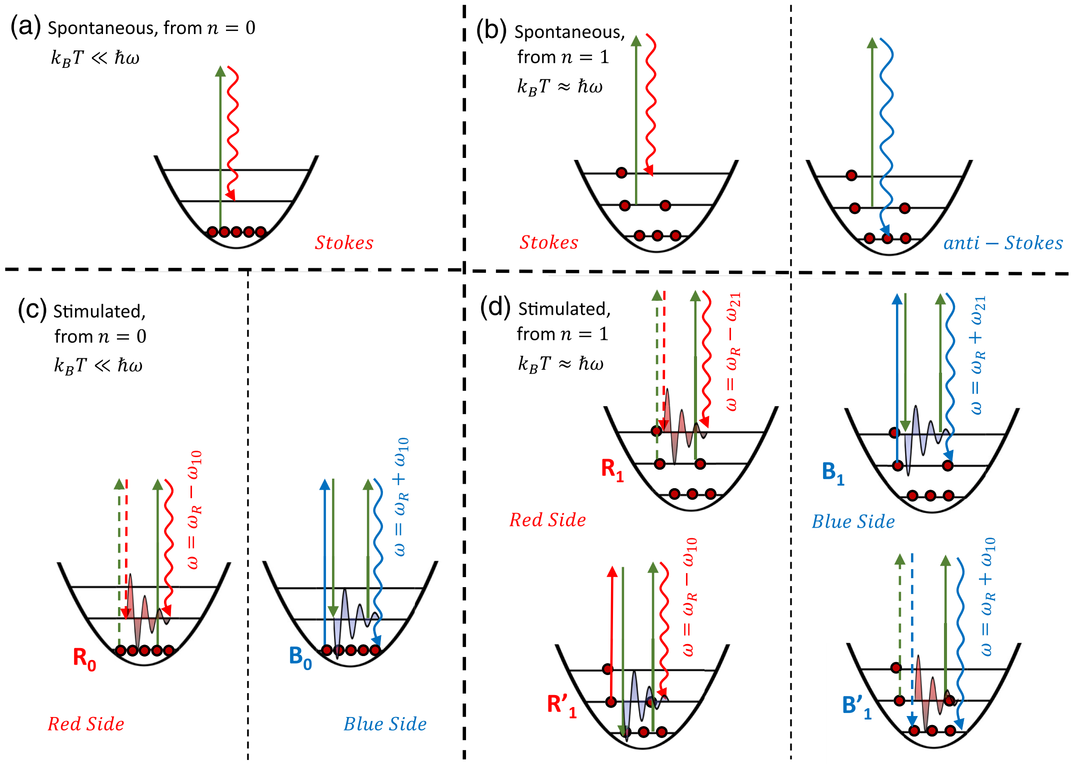

FIG. 1. Energy levels involved in Stokes and anti-Stokes SR processes from the ground or first excited vibrational levels (a)–(b). The corresponding pathways, describing the molecular density matrix evolution and the interaction with the electromagnetic fields, are shown in (c)–(d) for nonresonant SRS processes; dashed or solid lines indicate interactions with the bra or ket, respectively. For a molecule initially in the $n = 0$ level, two pathways (R_0/B_0) contribute to the SRS response, generating a peak (loss) in the red (blue) side. When the molecule is initially in the $n = 1$ state, additional pathways are enabled: R_1/B_1 are the natural extension of R_0/B_0 and probe the $|1\rangle \rightarrow |2\rangle$ transition, while R'_1/B'_1 involve the $|1\rangle \rightarrow |0\rangle$ transition. Spontaneous Stokes pathways correspond to R_i diagrams (leading to gains in the red side), whereas spontaneous anti-Stokes processes originate from B'_i diagrams (blue side gains). In both cases the vacuum field replaces the probe beam.

femtosecond Actinic pump, temporally preceding the RP-PP pair, turns SRS and ISRS into powerful pump-probe schemes, which represent ideal tools to track structural changes in ultrafast photochemical or photophysical processes [37–48].

In order to have a closer comparison with spontaneous Raman spectroscopy, we focus on frequency-domain SRS. The diagrams describing the radiation-matter interactions responsible for the signal generation of the former, indeed, coincide with a subset of the latter's. SRS experiments are sensitive to the third-order susceptibility, which is probed via the heterodyne detection of the induced nonlinear polarization $P^{(3)}$. Under the electronically nonresonant regime, i.e. when the pulses' wavelengths are detuned with respect to the sample absorption, the radiation-matter interaction Hamiltonian involved in preparing and detecting the vibrational coherences is [49,50] $H_I = -\alpha \cdot |E|^2$, where α is the molecular polarizability. The Raman response can be isolated from the spectrally resolved probe via the Raman gain $RG = I_P(\omega)/I_P^0(\omega) - 1$, where $I_P(\omega)$ ($I_P^0(\omega)$) indicates the PP spectrum recorded in presence (absence) of the RP. In Fig. 1(c), the pathways responsible for the SRS signals are reported for both the red (R_0 diagram) and the blue (B_0 diagram) side of the spectrum, considering a system initially in the ground state ($n = 0$). Briefly, in the R_0 process an interaction between the bra side of the density matrix and the RP is followed by an interaction with the PP, which brings the system to the $|0\rangle\langle 1|$ vibrational coherence. Then another interaction with the RP occurs on the ket side, preceding the free induction decay that leaves the system in the $|1\rangle\langle 1|$ population. In the B_0 process all the interactions occur on the ket side: the vibrational coherence is prepared by an interaction with a PP spectral component blueshifted with respect to the pump, degenerate with the emission frequency. Under the nonresonant regime, such processes give rise to the following polarizations [51,52]:

$$P_{R_0}(\omega) = -\frac{p_0}{\hbar}\left[\frac{\partial\alpha(T)}{\partial Q}\right]^2 |\langle 1|\hat{Q}|0\rangle|^2 \frac{|E_R|^2 E_P}{\omega_R - \omega_{10} - \omega - i\gamma_{10}}, \tag{1}$$

$$P_{B_0}(\omega)=\frac{p_0}{\hbar}\left[\frac{\partial\alpha(T)}{\partial Q}\right]^2|\langle 1|\hat{Q}|0\rangle|^2\frac{|E_R|^2E_P}{\omega_R+\omega_{10}-\omega-i\gamma_{10}}, \quad (2)$$

where γ_{ij} indicates the dephasing rate of the $|i\rangle\langle j|$ coherence, $\omega_{ij}=\omega_i-\omega_j$, p_j is the initial j-state population, $(\partial\alpha/\partial Q)$ is the molecular polarizability derivative (calculated at the equilibrium geometry) with respect to the considered normal coordinate Q, $E_{R/P}$ denotes the RP-PP field amplitude. Without loss of generality, we have considered an impulsive PP and a monochromatic RP. These polarizabilities can be exploited to compute the RG via the relation [53] $RG\propto-\Im[\omega P(\omega)/E_P(\omega)]$, valid in the low excitation regime [54]:

$$\mathrm{RG}_{R_0}(\omega)\propto p_0\left[\frac{\partial\alpha(T)}{\partial Q}\right]^2\frac{|\langle 1|\hat{Q}|0\rangle|^2}{\hbar}\frac{\omega\gamma_{10}|E_R|^2}{(\omega_R-\omega_{10}-\omega)^2+\gamma_{10}^2},$$

$$\mathrm{RG}_{B_0}(\omega)\propto -p_0\left[\frac{\partial\alpha(T)}{\partial Q}\right]^2\frac{|\langle 1|\hat{Q}|0\rangle|^2}{\hbar}\frac{\omega\gamma_{10}|E_R|^2}{(\omega_R+\omega_{10}-\omega)^2+\gamma_{10}^2}.$$

$\mathrm{RG}_{R_0}(\omega)$ corresponds to a positive red-side gain (at $\omega=\omega_R-\omega_{10}$), while $\mathrm{RG}_{B_0}(\omega)$ generates a negative blue-side loss (at $\omega=\omega_R+\omega_{10}$). The amplitude of both the signals is proportional to the polarizability derivative square modulus, the RP intensity $I_R=|E_R|^2$ and the $|\langle 1|\hat{Q}|0\rangle|^2$ wave functions overlap.

When the sample temperature increases, levels with a vibrational quantum number greater than 0 can be initially populated, enabling additional Raman transitions and potentially temperature dependent polarizability. An accurate calculation of the response function requires hence summing over all the contributions from thermally populated higher-lying levels. For instance, SRS probes $n=1\rightarrow n=2$ transitions via the following third-order polarization

$$P_{R_1}(\omega)=-\frac{p_1}{\hbar}\left[\frac{\partial\alpha(T)}{\partial Q}\right]^2|\langle 2|\hat{Q}|1\rangle|^2\frac{|E_R|^2E_P}{\omega_R-\omega_{21}-\omega-i\gamma_{21}},$$

which is formally analogous to Eq. (1) and gives rise to a positive peak at $\omega=\omega_R-\omega_{21}$. Similarly, in the blue side $n=1\rightarrow n=2$ transitions are probed by the following polarization:

$$P_{B_1}(\omega)=\frac{p_1}{\hbar}\left[\frac{\partial\alpha(T)}{\partial Q}\right]^2|\langle 2|\hat{Q}|1\rangle|^2\frac{|E_R|^2E_P}{\omega_R+\omega_{21}-\omega-i\gamma_{21}}.$$

Critically, permutations of the RP and PP fields are now possible giving also rise to the R_1' and B_1' pathways depicted in Fig. 1(d), involving the $|0\rangle\langle 1|$ and $|1\rangle\langle 0|$ vibrational coherences, respectively. The corresponding polarizations read as

$$P_{R_1'}(\omega)=\frac{p_1}{\hbar}\left[\frac{\partial\alpha(T)}{\partial Q}\right]^2|\langle 1|\hat{Q}|0\rangle|^2\frac{|E_R|^2E_P}{\omega_R-\omega_{10}-\omega-i\gamma_{10}},$$

$$P_{B_1'}(\omega)=-\frac{p_1}{\hbar}\left[\frac{\partial\alpha(T)}{\partial Q}\right]^2|\langle 1|\hat{Q}|0\rangle|^2\frac{|E_R|^2E_P}{\omega_R+\omega_{10}-\omega-i\gamma_{10}}.$$

Interestingly, the polarizations appearing in the R_1'-B_1' responses are identical to those observed in the R_0-B_0 pathways. However, the R_1'-B_1' intensities vary in amplitude (being proportional to the initial p_1 population) and, most importantly, exhibit opposite signs, leading to a destructive interference with the R_0-B_0 pathways. This can be rationalized as an effect analogous to the competition between stimulated emission and absorption processes in a two level system [55].

The measured SRS response can be finally derived by summing over the initial vibrational levels, weighted by the corresponding thermal populations. The resulting red and blue side RGs read

$$\mathrm{RG}_R(\omega)\propto\left[\frac{\partial\alpha(T)}{\partial Q}\right]^2\omega I_R\sum_{j=0}^{\infty}(p_j-p_{j+1})\frac{\gamma_j|\langle j+1|\hat{Q}|j\rangle|^2}{(\omega_R-\omega_j-\omega)^2+\gamma_j^2}, \quad (3)$$

$$\mathrm{RG}_B(\omega)\propto-\left[\frac{\partial\alpha(T)}{\partial Q}\right]^2\omega I_R\sum_{j=0}^{\infty}(p_j-p_{j+1})\frac{\gamma_j|\langle j+1|\hat{Q}|j\rangle|^2}{(\omega_R+\omega_j-\omega)^2+\gamma_j^2}, \quad (4)$$

where $p_j=(e^{-E_j/k_BT}/Z)$ and $Z=\sum_0^\infty e^{-E_j/k_BT}$ is the partition function. For improved readability, we have indicated $\omega_{j+1,j}$ and $\gamma_{j+1,j}$ as ω_j and γ_j. Equations (3) and (4) show the same dependence on the vibrational population, indicating that the ratio between the red and the blue side SRS responses is independent of temperature, rationalizing the results of Ref. [21] in terms of sum over the vibrational levels.

It is worth to stress that this result is valid also for large excitation regimes: high RP fluences can indeed result in larger RGs, once the exponential gain regime is initiated [54]. However, they do not alter the SRS sensitivity to the molecular properties, as the measured signal still depends on the same third-order polarization as $\mathrm{RG}_{R/B}(\omega)=e^{-\{2\pi\omega\Im[P^{(3)}_{R/B}(\omega)/E_P(\omega)]L/cn\}}-1$, where n, c, and L indicate the sample refractive index, the speed of light in vacuum, and sample length, respectively.

The spontaneous Raman case can be seen as a SRS process in which the probe pulse is provided by the vacuum field. Since this latter cannot be annihilated, only those pathways that contain two matter deexcitations into the vacuum field contributes to SR, corresponding to the diagrams where the last two interactions are complex conjugate of the first two (R_i and B_i').

This results in the well known Stokes (red side, with final level higher than the initial one) and anti-Stokes (blue side, with final state lower than the initial one) processes, naturally weighted by different thermal populations. The summation over all the possible directions of the scattered field leads to a cubic dependence of the spontaneous Raman cross section on the emitted frequency ω, in contrast with the linear dependence ruling stimulated processes [55]; the corresponding Stokes and anti-Stokes signals read

$$R_S(\omega) \propto \left[\frac{\partial\alpha(T)}{\partial Q}\right]^2 \omega^3 I_R \sum_{j=0}^{\infty} p_j \frac{\gamma_j |\langle j+1|\hat{Q}|j\rangle|^2}{(\omega_R-\omega_j-\omega)^2+\gamma_j^2}$$

$$R_{AS}(\omega) \propto \left[\frac{\partial\alpha(T)}{\partial Q}\right]^2 \omega^3 I_R \sum_{j=0}^{\infty} p_{j+1} \frac{\gamma_j |\langle j|\hat{Q}|j+1\rangle|^2}{(\omega_R+\omega_j-\omega)^2+\gamma_j^2}. \quad (5)$$

Summing up, for a given normal mode, both SRS and SR emit on the red and blue side depending on the relative wavelengths of the last two interactions, which scatter off the vibrational coherence. Critically, in SR the two cases can only originate from Stokes and anti-Stokes processes, respectively: therefore the measured response depends directly on the temperature via the thermal populations. In the stimulated regime this is no longer true: two Stokes contributions, originating from the coherently driven vibrational coherences, can be scattered off by different processes emitting on the red or blue side (R/B families in Fig. 1).

All the aforementioned considerations can also be applied to coherent Stokes and anti-Stokes Raman scattering and ISRS, with the distinction that the vibrational coherence preparation and the pulses are different [56–59]. The derivation of the corresponding polarizations is reported in the Supplemental Material [60].

To assess the effect of thermal excitations on spontaneous versus coherent Raman spectra, we start considering a simple harmonic molecular system, with frequency ω_v and a j-independent dephasing rate ($\gamma_j = \gamma_v$), evaluating the $\sum_{j=0}^{\infty} p_j$ summation. The thermal occupation numbers of the j levels are

$$p_j = \left(e^{-j\hbar\omega_v/(k_B T)}\right) \cdot \left(1 - e^{-\hbar\omega_v/(k_B T)}\right) \quad (6)$$

while

$$\Delta p_j = p_j - p_{j+1} = e^{-j\hbar\omega_v/(k_B T)} \cdot \left(1 - e^{-\hbar\omega_v/(k_B T)}\right)^2. \quad (7)$$

Finally, the transition amplitudes $\langle j+1|\hat{Q}|j\rangle$, $\langle j|\hat{Q}|j+1\rangle$ read

$$\langle j+1|\hat{Q}|j\rangle = \langle j+1|\sqrt{\frac{\hbar}{2m\omega_v}}(\hat{a}+\hat{a}^\dagger)|j\rangle = \sqrt{\frac{(j+1)\hbar}{2m\omega_v}},$$

$$\langle j|\hat{Q}|j+1\rangle = \langle j|\sqrt{\frac{\hbar}{2m\omega_v}}(\hat{a}+\hat{a}^\dagger)|j+1\rangle = \sqrt{\frac{(j+1)\hbar}{2m\omega_v}}, \quad (8)$$

which increase as the initial occupation number j is increased, critically determining the temperature dependence of spontaneous Raman responses. Plugging these relations into Eq. (5), the spontaneous Stokes response can be expressed as

$$R_S(\omega) \propto \left[\frac{\partial\alpha(T)}{\partial Q}\right]^2 \frac{\gamma_v \omega^3 I_R}{(\omega_R-\omega_v-\omega)^2+\gamma_v^2} \cdot \frac{\hbar}{2m\omega_v} \times \sum_{j=0}^{\infty} (j+1) \cdot e^{-j\hbar\omega_v/(k_B T)} \cdot \left(1 - e^{-\hbar\omega_v/(k_B T)}\right).$$

Carrying out the summation over the initial states j and incorporating the constant $(\hbar/2m\omega_v)$ term into the proportionality relation, $R_S(\omega)$ reads

$$R_S(\omega) \propto \left[\frac{\partial\alpha(T)}{\partial Q}\right]^2 \frac{\gamma_v \omega^3 I_R}{(\omega_R-\omega_v-\omega)^2+\gamma_v^2} \cdot (\langle n\rangle + 1), \quad (9)$$

where $\langle n\rangle = [1/(e^{\hbar\omega_v/(k_B T)} - 1)]$ is the mean occupation number. Similarly, $R_{AS}(\omega)$ reads

$$R_{AS}(\omega) \propto \left[\frac{\partial\alpha(T)}{\partial Q}\right]^2 \frac{\gamma_v \omega^3 I_R}{(\omega_R+\omega_v-\omega)^2+\gamma_v^2} \cdot \langle n\rangle. \quad (10)$$

On the other hand, the temperature dependence of the red and blue side SRS responses is ruled by the following summation:

$$\sum_{j=0}^{\infty} (p_j - p_{j+1}) \cdot (j+1) = \sum_{j=0}^{\infty} (j+1) \cdot e^{-j\hbar\omega_v/(k_B T)} \cdot \left(1 - e^{-\hbar\omega_v/(k_B T)}\right)^2 = 1.$$

Therefore, the Raman gains on the red and blue side can be expressed as

$$\mathrm{RG}_R(\omega) \propto \left[\frac{\partial\alpha(T)}{\partial Q}\right]^2 \cdot \frac{\gamma_v \omega I_R}{(\omega_R-\omega_v-\omega)^2+\gamma_v^2}, \quad (11)$$

$$\mathrm{RG}_B(\omega) \propto -\left[\frac{\partial\alpha(T)}{\partial Q}\right]^2 \cdot \frac{\gamma_v \omega I_R}{(\omega_R+\omega_v-\omega)^2+\gamma_v^2}, \quad (12)$$

notably, the only temperature dependence is brought about by the polarizability gradient. The same results can be obtained considering a temperature dependent dephasing rate, as the integrated Raman response intensities do not

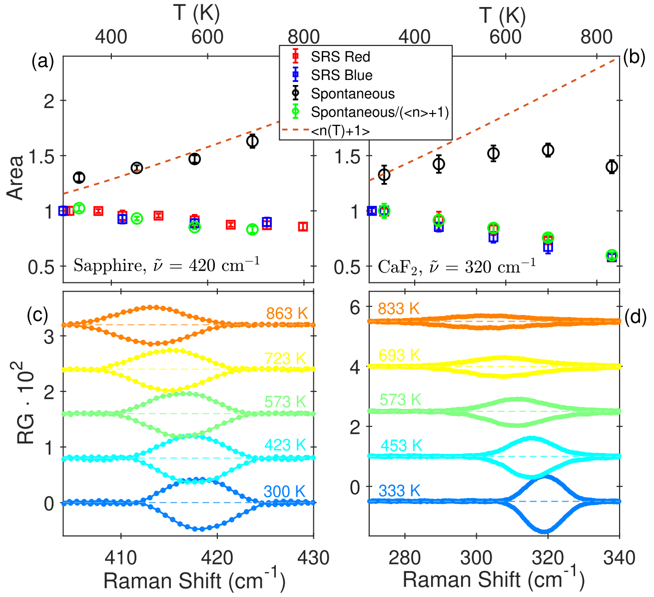

FIG. 2. Temperature dependence of spontaneous and stimulated Raman responses. Experimental responses have been measured for two crystals, namely, sapphire (band at ~420 cm^{-1}) and CaF$_2$ (at ~320 cm^{-1}), and are reported evaluating the peak areas in panels (a)–(b), respectively. SRS and SR areas (integrated intensities) divided by the occupation number ($\langle n\rangle + 1$) have been normalized by a constant factor to benchmark Eqs. (9), (11), and (12). Panels (c)–(d) show the corresponding SRS spectra, measured in the red (gains) and in the blue (losses) sides.

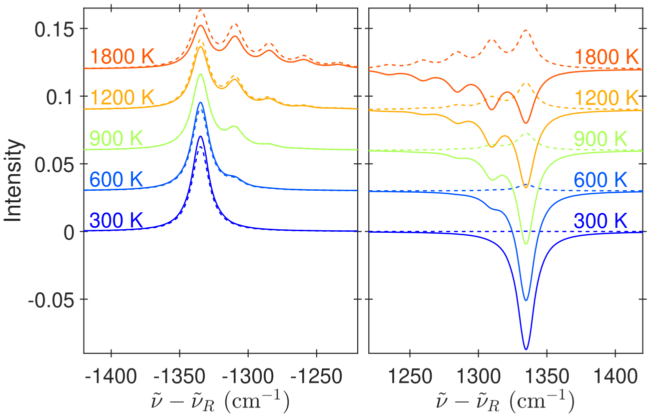

FIG. 3. Comparison of stimulated and spontaneous (solid and dashed lines) Raman responses as a function of temperature for a model Morse potential, with a fundamental band at 1335 cm^{-1}, constant dephasing rate $\gamma_v = 15$ cm^{-1}, and consecutive hot-band transitions shifted by 15 cm^{-1} [71]. SRS and SR spectra have been normalized to the same intensity at 900 K, assuming a monochromatic RP ($\lambda_{\mathrm{RP}} = 800$ nm) and a spectrally flat PP. For clarity, spectra at different temperatures are vertically offset.

depend on γ (details are reported in the Supplemental Material [60]).

To benchmark the presented theoretical results, SRS spectra have been measured for two crystals, namely, sapphire and CaF$_2$, as a function of temperature. The integrated area of the monitored bands (centered at ~420 and ~320 cm^{-1}, respectively) are reported in Fig. 2. Notably, the areas of sapphire and CaF$_2$ bands experience a reduction of approximately 10% and 40%, respectively, as the temperature increases from 300 to 800 K. To verify our theoretical prediction, we also measured the corresponding SR Stokes response over the same temperature range, which shows a significant deviation from the mean occupation number ($\langle n\rangle + 1$). Critically, by factoring out such dependence we find an excellent agreement with the SRS data, validating our results. This also indicates that in the harmonic limit the observed decreasing trend is a measure of the $|\partial\alpha(T)/\partial Q|$ temperature decrease.

The question now stands on whether coherent vibrational Raman can be used for thermometry. While it is well understood [21] that the red or blue side ratio is thermally inactive, our result indicates that a single spectral component features a temperature dependence brought about by the sample polarizability, even in the harmonic case. Exploiting such a dependence would require either a calibration or an *a priori* knowledge of $[\partial\alpha(T)/\partial Q]^2$. A convenient alternative is granted by anharmonic effects. A simple illustrative case is offered by single mode molecular anharmonicity, which is well captured by the Morse potential [69–71] model. As shown in Fig. 3, upon increasing temperature, the molecular redistribution over the energy levels affects both the polarizability and the vibrational spectrum with the appearance of the hot band progression. The former can be factored out by comparing, for example, the relative amplitudes of two adjacent components (an approach of practical interest when the hot bands can be resolved), which, from Eq. (7), is $\Delta p_{j+1}/\Delta p_j = e^{-\hbar\omega_v/(k_B T)}$.

In conclusion, we have studied the temperature dependence of Raman processes by combining a quantum description of matter with a perturbative expansion of the molecular density matrix. This approach allowed us to dissect how different transitions within the vibrational manifold participate to the scattering mechanism, providing a direct comparison between spontaneous and stimulated processes. Generally, molecular potentials exhibit Raman transition amplitudes that increase with the occupation number ($\langle j|\hat{Q}|j+1\rangle \propto \sqrt{j+1}$, for harmonic potentials): this makes spontaneous Raman enhanced by thermal fluctuations. The same molecular transitions, with the same transition amplitudes, are involved in coherent Raman spectroscopy and, hence, a dependence similar to SR may be erroneously expected also for CRS. However, due to the different permutations of the external electromagnetic fields participating to the radiation-matter interactions, additional pathways concur to the generation of CRS signals. In particular, stimulated processes originating from vibrationally excited energy levels can engage in destructive interference with transitions from the ground state or lower-lying energy levels, ultimately modifying the temperature dependence. In particular, the total cross section of CRS processes is less sensitive to thermal effects with respect to SR. In the specific case of a simple harmonic molecular potential, the nonresonant CRS response merely reflects the temperature dependence of the polarizability gradient, in sharp contrast with SR. For these reasons, stimulated Raman-based vibrational thermometry requires more refined methodologies, relying either on an *a priori* knowledge of the molecular polarizability or on the direct observation of anharmonic signatures.

Acknowledgments—This project has received funding from the Project ECS 0000024 Rome Technopole,—CUP B83C22002820006, NRP Mission 4 Component 2 Investment 1.5, Funded by the European Union—NextGenerationEU (T. S.). G. B. and T. S. acknowledge the "Progetti di Ricerca Medi 2021," the "Progetti di Ricerca Medi 2022" grants by Sapienza Universitá di Roma. E. M. and M. M. acknowledge the "Progetti di Avvio alla Ricerca 2022/2023" grants by Sapienza Universitá di Roma. S. M. acknowledges the support of NSF through Grant CHE-2246379. G. B. and T. S. acknowledge the support of EU HORIZON funding programme through Grant GA-101120832.

[1] C. Raman and K. S. Krishnan, A new type of secondary radiation, Nature (London) **121**, 501 (1928).
[2] M. Cardona and G. Güntherodt, *Light Scattering in Solids II* (Springer, Berlin Heidelberg, Berlin, 1982).
[3] U. Hohm and K. Kerl, Temperature dependence of mean molecular polarizability of gas molecules, Mol. Phys. **58**, 541 (1986).
[4] R. P. Bell, Polarisibility and internuclear distance, Trans. Faraday Soc. **38**, 422 (1942).
[5] R. Ananthakrishnan, Effect of temperature on the Raman spectrum of liquid CCl_4: Some preliminary considerations, Proc. Indian Acad. Sci. A **7**, 196 (1938).
[6] A. Quittet and M. Lambert, Temperature dependence of the Raman cross section and light absorption in cubic $BaTiO_3$, Solid State Commun. **12**, 1053 (1973).
[7] V. Mazzacurati, G. Ruocco, G. Signorelli, E. Cazzanelli, A. Fontana, and G. Mariotto, Theoretical model for the temperature dependence of Raman scattering in α-agi, Phys. Rev. B **26**, 2216 (1982).
[8] J. Menéndez and M. Cardona, Temperature dependence of the first-order Raman scattering by phonons in Si, ge, and $\alpha-$Sn: Anharmonic effects, Phys. Rev. B **29**, 2051 (1984).
[9] Y. I. Yuzyuk, Raman scattering spectra of ceramics, films, and superlattices of ferroelectric perovskites: A review, Phys. Solid State **54**, 1026 (2012).
[10] E. Meloche, M. G. Cottam, and D. J. Lockwood, One-magnon and exciton inelastic light scattering in the antiferromagnet CoF_2, Low Temp. Phys. **40**, 134 (2014).
[11] M. Kasperczyk, A. Jorio, E. Neu, P. Maletinsky, and L. Novotny, Stokes–anti-stokes correlations in diamond, Opt. Lett. **40**, 2393 (2015).
[12] S. Sandell, E. Chávez-Ángel, A. El Sachat, J. He, C. M. Sotomayor Torres, and J. Maire, Thermoreflectance techniques and Raman thermometry for thermal property characterization of nanostructures, J. Appl. Phys. **128**, 131101 (2020).
[13] K. Kumar, O. Stefanczyk, S. Chorazy, K. Nakabayashi, and S.-i. Ohkoshi, Ratiometric Raman and luminescent thermometers constructed from dysprosium thiocyanidometallate molecular magnets, Adv. Opt. Mater. **10**, 2201675 (2022).
[14] Y. Mizutani, Direct observation of cooling of heme upon photodissociation of carbonmonoxy myoglobin, Science **278**, 443 (1997).
[15] X. Ye, A. Demidov, F. Rosca, W. Wang, A. Kumar, D. Ionascu, L. Zhu, D. Barrick, D. Wharton, and P. M. Champion, Investigations of heme protein absorption line shapes, vibrational relaxation, and resonance Raman scattering on ultrafast time scales, J. Phys. Chem. A **107**, 8156 (2003).
[16] E. L. Keller and R. R. Frontiera, Ultrafast nanoscale Raman thermometry proves heating is not a primary mechanism for plasmon-driven photocatalysis, ACS Nano **12**, 5848 (2018).
[17] M. Soini, I. Zardo, E. Uccelli, S. Funk, G. Koblmüller, A. Fontcuberta i Morral, and G. Abstreiter, Thermal conductivity of GaAs nanowires studied by micro-Raman spectroscopy combined with laser heating, Appl. Phys. Lett. **97**, 263107 (2010).
[18] O. Braun, R. Furrer, P. Butti, K. Thodkar, I. Shorubalko, I. Zardo, M. Calame, and M. L. Perrin, Spatially mapping thermal transport in graphene by an opto-thermal method, npj 2D Mater. Appl. **6**, 6 (2022).
[19] B. Mallick, A. Lakhsmanna, and S. Umapathy, Ultrafast Raman loss spectroscopy (URLS): Instrumentation and principle, J. Raman Spectrosc. **42**, 1883 (2011).
[20] N. C. Dang, C. A. Bolme, D. S. Moore, and S. D. McGrane, Femtosecond stimulated Raman scattering picosecond molecular thermometry in condensed phases, Phys. Rev. Lett. **107**, 043001 (2011).
[21] U. Harbola, S. Umapathy, and S. Mukamel, Loss and gain signals in broadband stimulated-Raman spectra: Theoretical analysis, Phys. Rev. A **88**, 011801(R) (2013).
[22] S. Lee, D. Zhang, D. W. McCamant, P. Kukura, and R. A. Mathies, Theory of femtosecond stimulated Raman spectroscopy, J. Chem. Phys. **121**, 3632 (2004).
[23] K. E. Dorfman, B. P. Fingerhut, and S. Mukamel, Time-resolved broadband Raman spectroscopies: A unified six-wave-mixing representation, J. Chem. Phys. **139**, 124113 (2013).
[24] E. O. Potma and S. Mukamel, Theory of coherent Raman scattering, in *Coherent Raman Scattering Microscopy*, edited by J.-X. Cheng and X. S. Xie (CRC Press, Boca Raton, FL, 2012).

[25] R. C. Prince, R. R. Frontiera, and E. O. Potma, Stimulated Raman scattering: From bulk to nano, Chem. Rev. **117**, 5070 (2016).

[26] D. R. Dietze and R. A. Mathies, Femtosecond stimulated Raman spectroscopy, Chem. Phys. Chem. **17**, 1224 (2016).

[27] P. Kukura, D. W. McCamant, and R. A. Mathies, Femtosecond stimulated Raman spectroscopy, Annu. Rev. Phys. Chem. **58**, 461 (2007).

[28] C. Ferrante, G. Batignani, G. Fumero, E. Pontecorvo, A. Virga, L. C. Montemiglio, G. Cerullo, M. H. Vos, and T. Scopigno, Resonant broadband stimulated Raman scattering in myoglobin, J. Raman Spectrosc. **49**, 913 (2018).

[29] S. Ruhman, A. Joly, and K. Nelson, Coherent molecular vibrational motion observed in the time domain through impulsive stimulated Raman scattering, IEEE J. Quantum Electron. **24**, 460 (1988).

[30] H. Kuramochi and T. Tahara, Tracking ultrafast structural dynamics by time-domain Raman spectroscopy, J. Am. Chem. Soc. **143**, 9699 (2021).

[31] G. Batignani, E. Mai, G. Fumero, S. Mukamel, and T. Scopigno, Absolute excited state molecular geometries revealed by resonance Raman signals, Nat. Commun. **13**, 7770 (2022).

[32] E. Mai, P. Malakar, G. Batignani, M. Martinati, S. Ruhman, and T. Scopigno, Orchestrating nuclear dynamics in a permanganate doped crystal with chirped pump-probe spectroscopy, J. Phys. Chem. Lett. **15**, 6634 (2024).

[33] S. Takeuchi, S. Ruhman, T. Tsuneda, M. Chiba, T. Taketsugu, and T. Tahara, Spectroscopic tracking of structural evolution in ultrafast stilbene photoisomerization, Science **322**, 1073 (2008).

[34] M. Liebel, C. Schnedermann, T. Wende, and P. Kukura, Principles and applications of broadband impulsive vibrational spectroscopy, J. Phys. Chem. A **119**, 9506 (2015).

[35] G. Batignani, C. Sansone, C. Ferrante, G. Fumero, S. Mukamel, and T. Scopigno, Excited-state energy surfaces in molecules revealed by impulsive stimulated Raman excitation profiles, J. Phys. Chem. Lett. **12**, 9239 (2021).

[36] G. Batignani, C. Ferrante, G. Fumero, M. Martinati, and T. Scopigno, Femtosecond stimulated Raman spectroscopy, Nat. Rev. Methods Primers **4**, 34 (2024).

[37] F. Provencher, N. Bérubé, A. W. Parker, G. M. Greetham, M. Towrie, C. Hellmann, M. Côté, N. Stingelin, C. Silva, and S. C. Hayes, Direct observation of ultrafast long-range charge separation at polymer-fullerene heterojunctions, Nat. Commun. **5**, 4288 (2014).

[38] G. Batignani, D. Bossini, N. D. Palo, C. Ferrante, E. Pontecorvo, G. Cerullo, A. Kimel, and T. Scopigno, Probing ultrafast photo-induced dynamics of the exchange energy in a Heisenberg antiferromagnet, Nat. Photonics **9**, 506 (2015).

[39] J. Zhou, W. Yu, and A. E. Bragg, Structural relaxation of photoexcited quaterthiophenes probed with vibrational specificity, J. Phys. Chem. Lett. **6**, 3496 (2015).

[40] G. Batignani, E. Pontecorvo, C. Ferrante, M. Aschi, C. G. Elles, and T. Scopigno, Visualizing excited-state dynamics of a diaryl thiophene: Femtosecond stimulated Raman scattering as a probe of conjugated molecules, J. Phys. Chem. Lett. **7**, 2981 (2016).

[41] M. S. Barclay, T. J. Quincy, D. B. Williams-Young, M. Caricato, and C. G. Elles, Accurate assignments of excited-state resonance Raman spectra: A benchmark study combining experiment and theory, J. Phys. Chem. A **121**, 7937 (2017).

[42] T. Takaya, M. Anan, and K. Iwata, Vibrational relaxation dynamics of β-carotene and its derivatives with substituents on terminal rings in electronically excited states as studied by femtosecond time-resolved stimulated Raman spectroscopy in the near-IR region, Phys. Chem. Chem. Phys. **20**, 3320 (2018).

[43] Y. Hontani, M. Kloz, T. Polívka, M. K. Shukla, R. Sobotka, and J. T. M. Kennis, Molecular origin of photoprotection in cyanobacteria probed by watermarked femtosecond stimulated Raman spectroscopy, J. Phys. Chem. Lett. **9**, 1788 (2018).

[44] Z. Piontkowski and D. W. McCamant, Excited-state planarization in donor-bridge dye sensitizers: Phenylene versus thiophene bridges, J. Am. Chem. Soc. **140**, 11046 (2018).

[45] C. Fang, L. Tang, and C. Chen, Unveiling coupled electronic and vibrational motions of chromophores in condensed phases, J. Chem. Phys. **151**, 200901 (2019).

[46] T. Fujisawa, H. Kuramochi, H. Hosoi, S. Takeuchi, and T. Tahara, Role of coherent low-frequency motion in excited-state proton transfer of green fluorescent protein studied by time-resolved impulsive stimulated Raman spectroscopy, J. Am. Chem. Soc. **138**, 3942 (2016).

[47] W. Kim and A. J. Musser, Tracking ultrafast reactions in organic materials through vibrational coherence: Vibronic coupling mechanisms in singlet fission, Adv. Phys. **6**, 1918022 (2021).

[48] R. Borrego-Varillas, A. Nenov, P. Kabaciński, I. Conti, L. Ganzer, A. Oriana, V. K. Jaiswal, I. Delfino, O. Weingart, C. Manzoni, I. Rivalta, M. Garavelli, and G. Cerullo, Tracking excited state decay mechanisms of pyrimidine nucleosides in real time, Nat. Commun. **12**, 7285 (2021).

[49] Y. Tanimura and S. Mukamel, Two-dimensional femtosecond vibrational spectroscopy of liquids, J. Chem. Phys. **99**, 9496 (1993).

[50] S. Mukamel, Controlling multidimensional off-resonant-Raman and infrared vibrational spectroscopy by finite pulse band shapes, J. Chem. Phys. **130**, 054110 (2009).

[51] G. Batignani, E. Pontecorvo, G. Giovannetti, C. Ferrante, G. Fumero, and T. Scopigno, Electronic resonances in broadband stimulated Raman spectroscopy, Sci. Rep. **6**, 18445 (2016).

[52] G. Batignani, C. Ferrante, and T. Scopigno, Accessing excited state molecular vibrations by femtosecond stimulated Raman spectroscopy, J. Phys. Chem. Lett. **11**, 7805 (2020).

[53] S. Mukamel, *Principles of Nonlinear Spectroscopy* (Oxford University Press, New York, 1995).

[54] G. Batignani, G. Fumero, E. Mai, M. Martinati, and T. Scopigno, Stimulated Raman lineshapes in the large light–matter interaction limit, Opt. Mater. X **13**, 100134 (2022).

[55] R. Loudon, *The Quantum Theory of Light* (Oxford University Press, New York, 2000).

[56] L. Monacelli, G. Batignani, G. Fumero, C. Ferrante, S. Mukamel, and T. Scopigno, Manipulating impulsive stimulated Raman spectroscopy with a chirped probe pulse, J. Phys. Chem. Lett. **8**, 966 (2017).

[57] D. Polli, V. Kumar, C. M. Valensise, M. Marangoni, and G. Cerullo, Broadband coherent Raman scattering microscopy, Laser Photonics Rev. **12**, 1800020 (2018).

[58] A. Virga, C. Ferrante, G. Batignani, D. D. Fazio, A. D. G. Nunn, A. C. Ferrari, G. Cerullo, and T. Scopigno, Coherent anti-stokes Raman spectroscopy of single and multi-layer graphene, Nat. Commun. **10**, 3658 (2019).

[59] G. Batignani, C. Ferrante, G. Fumero, and T. Scopigno, Broadband impulsive stimulated Raman scattering based on a chirped detection, J. Phys. Chem. Lett. **10**, 7789 (2019).

[60] See Supplemental Material at http://link.aps.org/supplemental/10.1103/PhysRevLett.133.206902, which includes Refs. [61–68], for additional information about the experimental methods and a detailed discussion of the theoretical derivations, including the case of coherent anti-stokes, Stokes, and impulsive Raman responses.

[61] I. Gdor, T. Ghosh, O. Lioubashevski, and S. Ruhman, Nonresonant Raman effects on femtosecond pump–probe with chirped white light: Challenges and opportunities, J. Phys. Chem. Lett. **8**, 1920 (2017).

[62] J. T. Fourkas, H. Kawashima, and K. A. Nelson, Theory of nonlinear optical experiments with harmonic oscillators, J. Chem. Phys. **103**, 4393 (1995).

[63] V. Kemlin, A. Bonvalet, L. Daniault, and M. Joffre, Transient two-dimensional infrared spectroscopy in a vibrational ladder, J. Phys. Chem. Lett. **7**, 3377 (2016).

[64] G. Batignani, G. Fumero, E. Pontecorvo, C. Ferrante, S. Mukamel, and T. Scopigno, Genuine dynamics vs cross phase modulation artefacts in femtosecond stimulated Raman spectroscopy, ACS Photonics **6**, 492 (2019).

[65] C. Manzoni and G. Cerullo, Design criteria for ultrafast optical parametric amplifiers, J. Opt. **18**, 103501 (2016).

[66] M. A. Marangoni, D. Brida, M. Quintavalle, G. Cirmi, F. M. Pigozzo, C. Manzoni, F. Baronio, A. D. Capobianco, and G. Cerullo, Narrow-bandwidth picosecond pulses by spectral compression of femtosecond pulses in second-order nonlinear crystals, Opt. Express **15**, 8884 (2007).

[67] E. Pontecorvo, S. Kapetanaki, M. Badioli, D. Brida, M. Marangoni, G. Cerullo, and T. Scopigno, Femtosecond stimulated Raman spectrometer in the 320–520 nm range, Opt. Express **19**, 1107 (2011).

[68] E. Pontecorvo, C. Ferrante, C. G. Elles, and T. Scopigno, Spectrally tailored narrowband pulses for femtosecond stimulated Raman spectroscopy in the range 330–750 nm, Opt. Express **21**, 6866 (2013).

[69] J. P. Dahl and M. Springborg, The Morse oscillator in position space, momentum space, and phase space, J. Chem. Phys. **88**, 4535 (1988).

[70] C. Ferrante, E. Pontecorvo, G. Cerullo, M. H. Vos, and T. Scopigno, Direct observation of subpicosecond vibrational dynamics in photoexcited myoglobin, Nat. Chem. **8**, 1137 (2016).

[71] C. Ferrante, G. Batignani, E. Pontecorvo, L. C. Montemiglio, M. H. Vos, and T. Scopigno, Ultrafast dynamics and vibrational relaxation in six-coordinate heme proteins revealed by femtosecond stimulated Raman spectroscopy, J. Am. Chem. Soc. **142**, 2285 (2020).

Supplemental Material: Temperature dependence of Coherent versus spontaneous Raman Scattering

Giovanni Batignani[1,2], Emanuele Mai[1,2], Miles Martinati[1],
Mohanan M. Neethish[1], Shaul Mukamel[3], Tullio Scopigno[1,2,4],
[1] *Dipartimento di Fisica, Universitá di Roma "La Sapienza", Roma, I-00185, Italy*
[2] *Center for Life Nano Science @Sapienza, Istituto Italiano di Tecnologia, Viale Regina Elena 291, I-00161, Roma,Italy*
[3] *Department of Chemistry, University of California, Irvine, 92623, California, USA and*
[4] *Istituto Italiano di Tecnologia, Graphene Labs, Via Morego 30, I-16163 Genova, Italy**
(Dated: October 29, 2024)

TEMPERATURE DEPENDENCE OF IMPULSIVE STIMULATED RAMAN SPECTROSCOPY

The pathways responsible for the ISRS signals are reported in Fig. 1: when the molecular system is initially in the ground state $n = 0$, only two processes (labeled as A_0 and B_0) contribute to the off-resonant ISRS signal generation [1]. Briefly, two interactions, either on the bra or on the ket side, with the femtosecond RP stimulate a vibrational coherence, and are followed by an interaction with the temporally delayed broadband PP and a free-induction decay. From a physical point of view, the first two interactions create a vibrational coherence while the last two represent the scattering of that coherence via Stokes and anti-Stokes processes: due to the field driven (athermal) vibrational excitation, the relative energy transfer between the red and the blue PP spectral components (originated by the two diagrams A_0 and B_0) is temperature independent. Importantly, due to the different state of the density matrix ($|1\rangle\langle 0|$ versus $|0\rangle\langle 1|$ for A_0 and B_0 processes, respectively) prepared by the RP, the two pathways generate time-domain responses which are out of phase and involve an interaction with a different PP spectral component: in the PP impulsive limit, this results in a vanishing off-resonant ISRS response. However, a proper control of the temporal delay between the PP spectral components, simply achieved by tuning the pulse chirp [2, 3], can be exploited to introduce an arbitrary phase between the A_0 and B_0 processes, ensuring strong ISRS signals, with a mode-specific enhancement [1, 4]. When the system is initially in a vibrationally excited population $|i\rangle\langle i|$, 4 pathways should be considered to evaluate the contribution to the measured response (in Fig. 1 they are illustrated for $i = 1$): A_i and B_i are the natural extension of the A_0 and B_0 pathways probing the $|i+1\rangle\langle i|$ vs $|i\rangle\langle i+1|$ coherences. On the contrary, A'_i and B'_i probe the $|i\rangle\langle i-1|$ and the $|i-1\rangle\langle i|$ coherences. The corresponding differential Raman gains, generated outside the pulse temporal overlap [5], can be evaluated as

$$S_{A_i}(\omega,T) \propto -p_i \left(\frac{\partial\alpha(T)}{\partial Q}\right)^2 |\langle i+1|\hat{Q}|i\rangle|^2 \cdot \Re\Big[E_P(\omega-\omega_i)/E_P(\omega)\hat{I}_R(\omega_i)e^{-i\omega_i T}\Big] \tag{S1}$$

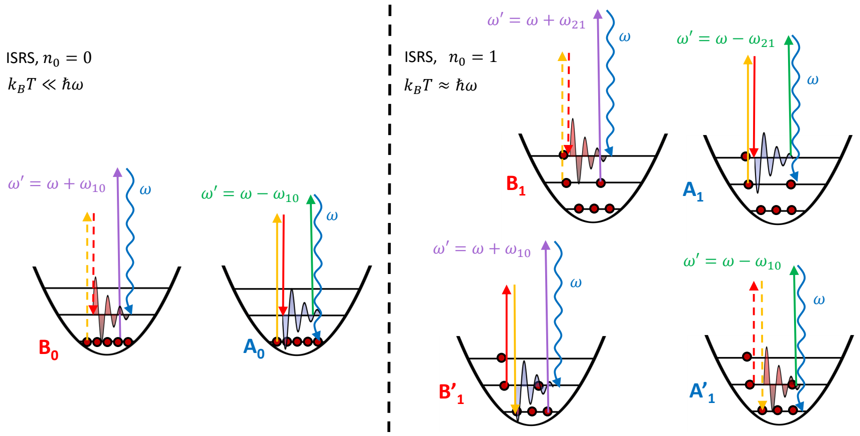

Supplementary Figure 1. Pathways responsible for ISRS processes from the ground ($n = 0$, left panel) and the first vibrationally excited ($n = 1$, right panel) state are compared. For a molecule initially in the $n = 0$ level, under the off-resonant regime only two pathways, labeled as B_0 and A_0, concur to the generation of the SRS response. When the molecule is initially in the $n = 1$ state, additional pathways are enabled: B_1 and A_1 are the natural extension of B_0 and A_0 and probe the $|1\rangle \rightarrow |2\rangle$ transition, while B'_1 and A'_1 involve the $|0\rangle\langle 1|$ and the $|1\rangle\langle 0|$ coherences, respectively

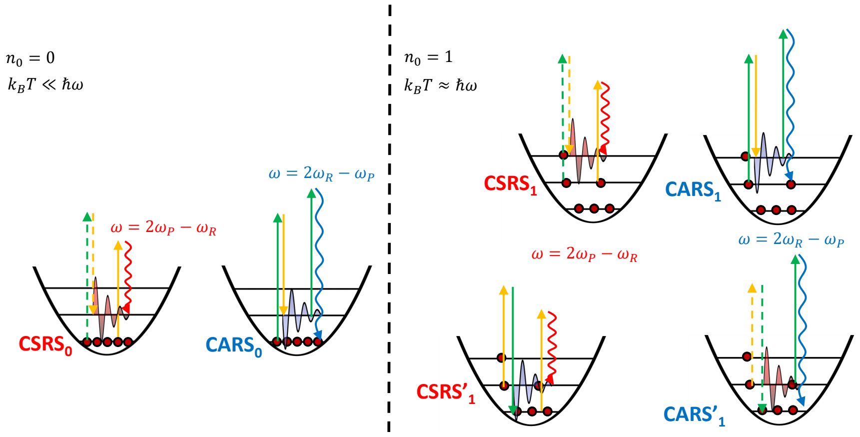

Supplementary Figure 2. Pathways responsible for CSRS and CARS processes from the ground ($n = 0$, left panel) and the first vibrationally excited ($n = 1$, right panel) state are compared. For a molecule initially in the $n = 0$ level, under the off-resonant regime there is only one process contributing to CSRS$_0$ and one to CARS$_0$. If the molecule is initially in the $n = 1$ state, additional pathways are enabled: CSRS$_1$ and CARS$_1$ are the natural extension of the former ones and probe the $|1\rangle \rightarrow |2\rangle$ transition, while CSRS$'_1$ and CARS$'_1$ involve the $|0\rangle\langle 1|$ and the $|1\rangle\langle 0|$ coherences, respectively

$$S_{B_i}(\omega, T) \propto +p_i \left(\frac{\partial\alpha(T)}{\partial Q}\right)^2 |\langle i+1|\,\hat{Q}\,|i\rangle|^2 \cdot \Re\Big[E_P(\omega+\omega_i)/E_P(\omega)\hat{I}_R(\omega_i)e^{+i\omega_i T}\Big] \tag{S2}$$

$$S_{A'_i}(\omega, T) \propto +p_i \left(\frac{\partial\alpha(T)}{\partial Q}\right)^2 |\langle i|\,\hat{Q}\,|i-1\rangle|^2 \cdot \Re\Big[E_P(\omega-\omega_{i-1})/E_P(\omega)\hat{I}_R(\omega_{i-1}))e^{-i\omega_{i-1} T}\Big] \tag{S3}$$

$$S_{B'_i}(\omega, T) \propto -p_i \left(\frac{\partial\alpha(T)}{\partial Q}\right)^2 |\langle i|\,\hat{Q}\,|i-1\rangle|^2 \cdot \Re\Big[E_P(\omega+\omega_{i-1})/E_P(\omega)\hat{I}_R(\omega_{i-1})e^{+i\omega_{i-1} T}\Big] \tag{S4}$$

where for simplicity we have assumed a vanishing dephasing rate, $I_R(\omega) = \int_{-\infty}^{+\infty} dt|E_R(t)|^2 e^{+i\omega t}$ denotes the Fourier transform of the RP temporal profile and T is the temporal delay between the RP and PP. Fourier transforming over T allows for retrieving the vibrational spectrum in the frequency domain, obtaining a response equivalent to SRS. In close analogy with the pathways discussed for frequency-domain SRS responses, the A'_{i+1}/B'_{i+1} processes probe the same molecular polarizabilities as the A_i/B_i processes, exhibiting different (population) amplitudes and opposite signs, which lead to a destructive interference.

TEMPERATURE DEPENDENCE OF CARS AND CSRS SPECTROSCOPIES

Energy level diagrams pertaining to the CSRS and CARS processes are illustrated in Supplementary Figure 2. In their simplest version, two narrowband pulses at frequencies ω_R and ω_P (with $\omega_R - \omega_P \approx \omega_v$) are exploited to record signals at $2\omega_P - \omega_R$ and $2\omega_R - \omega_P$, respectively [6]. Since the emitted signals occur at frequencies that are different with respect to the input beams, CSRS and CARS are homodyne techniques, accessing the square modulus of the third-order polarizability [7, 8]. When the molecular system is initially in the ground state, they read as

$$P_{CSRS_0}(\omega) = -\frac{p_0}{\hbar}\left(\frac{\partial\alpha(T)}{\partial Q}\right)^2 I_P E_R |\langle 0|\,\hat{Q}\,|1\rangle|^2 \frac{2\pi\delta(\omega+\omega_R-2\omega_P)}{\omega_P-\omega_{10}-\omega-i\gamma_{10}}$$

and

$$P_{CARS_0}(\omega) = \frac{p_0}{\hbar}\left(\frac{\partial\alpha(T)}{\partial Q}\right)^2 I_R E_P |\langle 0|\,\hat{Q}\,|1\rangle|^2 \frac{2\pi\delta(2\omega_R-\omega_P-\omega)}{\omega_R+\omega_{10}-\omega-i\gamma_{10}}$$

where the Dirac deltas originate from the energy conservation and from assuming monochromatic pulses. Similarly to SRS and ISRS, as the temperature is raised additional pathways, originated by the initial population in the $i > 0$

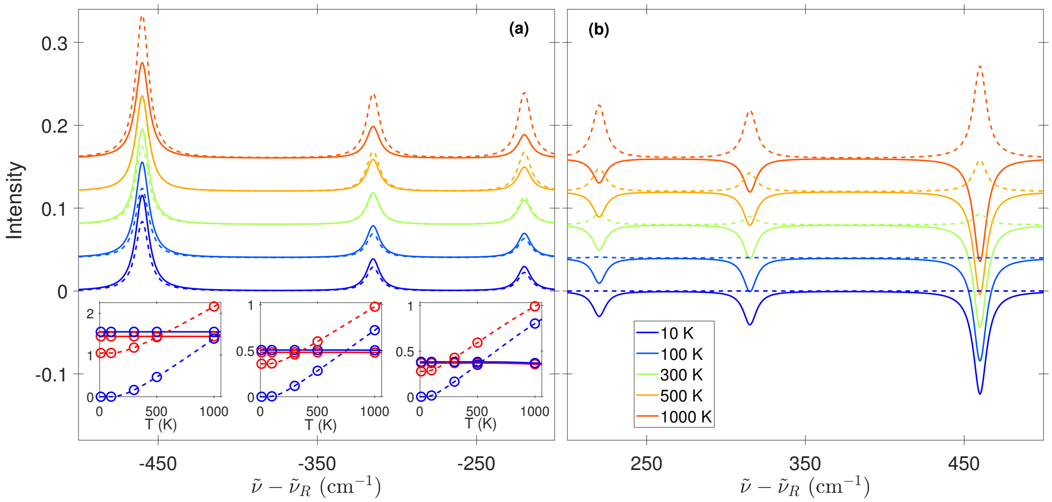

Supplementary Figure 3. Comparison of stimulated/spontaneous (solid/dashed lines) Raman responses as a function of temperature for a model harmonic molecular system, with three normal modes (at 220, 315 and 460 cm^{-1}, with $\gamma_j = 7$ cm^{-1}) and a temperature-independent polarizability. A monochromatic RP ($\lambda_{RP} = 800$ nm) and a spectrally flat PP are assumed. The red-side SRS spectrum is reported in (a) with the Stokes spontaneous contribution, while the blue-side is shown in (b) with the anti-Stokes. In the insets, the areas of the different signals are compared as a function of the sample temperature (solid red/blue lines indicate the SRS areas, dashed red/blue lines the Stokes/anti-Stokes spontaneous areas).

levels, contribute to the measured signals generating the following polarizabilities:

$$P_{CSRS_i}(\omega) = -\frac{p_i}{\hbar}\left(\frac{\partial\alpha(T)}{\partial Q}\right)^2 I_P E_R |\langle i|\hat{Q}|i+1\rangle|^2 \frac{2\pi\delta(\omega+\omega_R-2\omega_P)}{\omega_P-\omega_i-\omega-i\gamma_i} \tag{S5}$$

and

$$P_{CARS_i}(\omega) = \frac{p_i}{\hbar}\left(\frac{\partial\alpha(T)}{\partial Q}\right)^2 I_R E_P |\langle i|\hat{Q}|i+1\rangle|^2 \frac{2\pi\delta(2\omega_R-\omega_P-\omega)}{\omega_R+\omega_i-\omega-i\gamma_i} \tag{S6}$$

$$P_{CSRS'_i}(\omega) = \frac{p_i}{\hbar}\left(\frac{\partial\alpha(T)}{\partial Q}\right)^2 I_P E_R |\langle i|\hat{Q}|i-1\rangle|^2 \frac{2\pi\delta(\omega+\omega_R-2\omega_P)}{\omega_P-\omega_{i-1}-\omega-i\gamma_{i-1}} \tag{S7}$$

and

$$P_{CARS'_i}(\omega) = -\frac{p_i}{\hbar}\left(\frac{\partial\alpha(T)}{\partial Q}\right)^2 I_R E_P |\langle i|\hat{Q}|i-1\rangle|^2 \frac{2\pi\delta(2\omega_R-\omega_P-\omega)}{\omega_R+\omega_{i-1}-\omega-i\gamma_{i-1}} \tag{S8}$$

Thus, the population initially in the i state can undergo two processes: it can be promoted to the $|i\rangle\langle i+1|$ and $|i+1\rangle\langle i|$ coherences, corresponding to the P_{CSRS_i} and P_{CARS_i} polarization, or it can undergo de-excitation to the $|i-1\rangle\langle i|$ and $|i\rangle\langle i-1|$ coherences. These pathways are associated to third-order polarizations $P_{CSRS'_i}$ and $P_{CARS'_i}$, that have opposite sign with respect to $P_{CSRS_{i-1}}$ and $P_{CARS_{i-1}}$, resulting in destructive interference.

SPECTRAL RESPONSE AND DEPHASING RATE

A comparison of the SR/SRS temperature-dependence computed using Eqs. 9-12 of the main text is reported in Supplementary Fig. 3a-b, for an ideal harmonic system with 3 normal modes. All the molecular parameters (excluding p_j) are assumed to be temperature independent. As it is well known, thermal population can affect the relative intensity of different vibrational modes measured by SR spectroscopy, due to the mode-specific enhancement of the cross-section ($\langle n\rangle + 1 = \frac{e^{\hbar\omega_v/(k_BT)}}{e^{\hbar\omega_v/(k_BT)}-1}$ and $\langle n\rangle = \frac{1}{e^{\hbar\omega_v/(k_BT)}-1}$ factors for Stokes and anti-Stokes sides, respectively). Remarkably, this is not the case for coherent Raman signals: upon increasing the vibrational level, the cross section enhancement is exactly compensated by the contribution of the additional pathways. The different behaviour of

SR and SRS with temperature is illustrated by evaluating the areas of each Raman band reported in the insets of Fig. 3a-b.

The interaction of the system with the surrounding environment may increase the dephasing rate of the vibrational coherences involving large occupation numbers [9], inducing a temperature dependent spectral broadening. This effect is evaluated in Supplementary Fig. 4a-b, where the spontaneous and stimulated Raman responses are evaluated for a model system with the dephasing rate that scales linearly with the occupation number [10] ($\gamma_j = \gamma_0 \cdot [j+1]$). All the other molecular parameters are the same as the harmonic system considered in Supplementary Fig.3. Critically, both the spontaneous and the SRS responses experience a spectral broadening as the temperature increases, accompanied by a consistent reduction in the peak amplitudes for the SRS signals. Also in this case, the areas of the measured Raman bands reveal a flat dependence of red/blue side SRS responses.

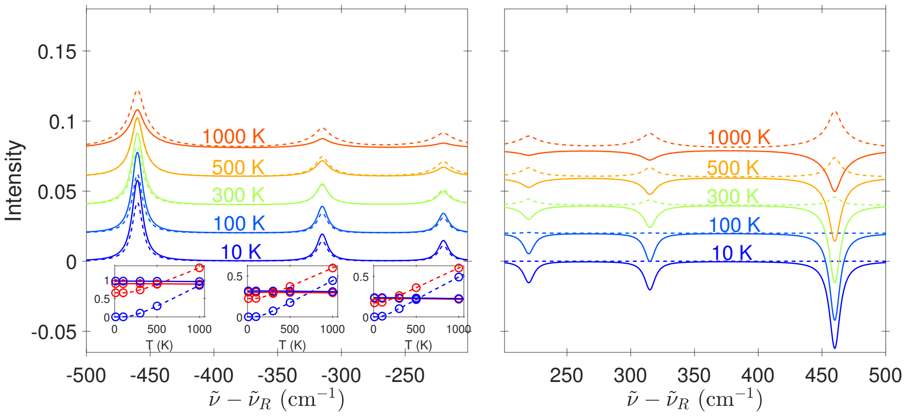

Supplementary Figure 4. Comparison of stimulated (solid lines) and spontaneous (dashed lines) Raman responses as a function of temperature for a harmonic molecular system, with three normal modes (at 220, 315 and 460 cm^{-1}), and a temperature-independent polarizability. A dephasing rate proportional to the occupation number ($\gamma_j = [j+1] \cdot 7$ cm^{-1}) has been assumed. A monochromatic RP ($\lambda_{RP} = 800$ nm) and a spectrally flat PP are considered. The red-side SRS spectrum is reported in (a) with the Stokes spontaneous contribution, while the blue-side is shown in (b) with the anti-Stokes.

INTENSITIES OF SINGLE RAMAN BANDS

A comparison of SR and SRS band intensities associated to a given initial vibrational level can be obtained combining the Eqs. reported in the main manuscript for red/blue and Stokes/anti-Stokes responses [3-5], here reported for clarity

$$RG_R(\omega) \propto \left[\frac{\partial\alpha(T)}{\partial Q}\right]^2 \omega I_R \sum_{j=0}^{\infty}(p_j - p_{j+1}) \frac{\gamma_j |\langle j+1|\hat{Q}|j\rangle|^2}{(\omega_R - \omega_j - \omega)^2 + \gamma_j^2} \tag{S9}$$

$$RG_B(\omega) \propto -\left[\frac{\partial\alpha(T)}{\partial Q}\right]^2 \omega I_R \sum_{j=0}^{\infty}(p_j - p_{j+1}) \frac{\gamma_j |\langle j+1|\hat{Q}|j\rangle|^2}{(\omega_R + \omega_j - \omega)^2 + \gamma_j^2} \tag{S10}$$

$$R_S(\omega) \propto \left[\frac{\partial\alpha(T)}{\partial Q}\right]^2 \omega^3 I_R \sum_{j=0}^{\infty} p_j \frac{\gamma_j |\langle j+1|\hat{Q}|j\rangle|^2}{(\omega_R - \omega_j - \omega)^2 + \gamma_j^2} \tag{S11}$$

$$R_{AS}(\omega) \propto \left[\frac{\partial\alpha(T)}{\partial Q}\right]^2 \omega^3 I_R \sum_{j=0}^{\infty} p_{j+1} \frac{\gamma_j |\langle j|\hat{Q}|j+1\rangle|^2}{(\omega_R + \omega_j - \omega)^2 + \gamma_j^2} \tag{S12}$$

with the population factors (p_j and $p_j - p_{j+1}$) in Eqs. [6-7] of the main manuscript, namely

$$p_j = e^{-E_j/k_B T} \cdot Z^{-1}$$

$$\Delta p_j = p_j - p_{j+1} = e^{-j\hbar\omega_v/(k_B T)} \cdot Z^{-2}$$

where $Z = \sum_0^\infty e^{-E_j/k_B T} \approx \frac{1}{1-e^{\hbar\omega_v/(k_B T)}}$. For the Stokes and red-side spectra, we obtain

$$R_S(\omega) \;\propto\; \left[\frac{\partial\alpha(T)}{\partial Q}\right]^2 \omega^3 I_R \sum_{j=0}^{\infty} \left(e^{-j\hbar\omega_v/(k_B T)}\right) \cdot Z^{-1} \frac{\gamma_j \left|\left\langle j+1|\hat{Q}|j\right\rangle\right|^2}{\left(\omega_R-\omega_j-\omega\right)^2+\gamma_j^2}$$

$$RG_R(\omega) \propto \left[\frac{\partial\alpha(T)}{\partial Q}\right]^2 \omega I_R \sum_{j=0}^{\infty} \left(e^{-j\hbar\omega_v/(k_B T)}\right) \cdot Z^{-2} \frac{\gamma_j \left|\left\langle j+1|\hat{Q}|j\right\rangle\right|^2}{\left(\omega_R-\omega_j-\omega\right)^2+\gamma_j^2}$$

Interestingly, except for the different scaling with the emitted frequency (ω^3 vs ω for spontaneous vs stimulated Raman signals, respectively), the intensity of the Stokes and SRS lines differ for a factor Z, which corresponds to the Bose term.

POLARIZABILITY TEMPERATURE DEPENDENCE

For a single normal mode (for example in the case of a diatomic molecule) the molecular polarizability α depends on the vibrational state j via the quantum average over the vibrational wavefunction $\psi_j(Q)$ reading as

$$\alpha_j = \int_{-\infty}^{+\infty} dQ|\psi_j(Q)|^2\alpha(Q) = \langle j|\,\hat{\alpha}\,|j\rangle \approx \alpha(Q_{\text{ave}}(j))$$

By averaging α_j over the thermal occupation of the vibrational states p_j, $\alpha(T)$ can be obtained as

$$\alpha(T) = \sum_{j=0}^{\infty} p_j\alpha_j$$

As discussed in [11], in the presence of an asymmetrical nature of the potential energy curve, $Q_{\text{ave}}(j)$ increases with the vibrational quantum number. For instance, considering a simple diatomic molecule with a potential energy curve $V(Q)$ asymmetric around its minimum, the equilibrium distance of the two nuclei, $Q_{\text{eq}}(T)$, depends on the temperature and it is different with respect to the minimum Q_0 of the nuclear potential $V(Q)$. Practically, $Q_{\text{eq}}(T)$ can be obtained by averaging $Q_{\text{ave}}(j)$ over all vibrational quantum numbers weighted by the corresponding occupation factors, obtaining slightly larger atomic distances at higher temperatures. As the molecular polarizability shows only weak modification across the interatomic distances explored via thermal fluctuations, the $\alpha(T)$ dependence is relatively small and this effect is generally negligible [11].

Similar considerations can be applied to larger molecules; indeed, for M vibrational degrees of freedom, the molecular polarizability depends on the vibrational states j_1, j_2, …, j_M, via the quantum average over the vibrational wavefunctions $\psi_1(Q_1)$, …, $\psi_M(Q_M)$, as

$$\begin{aligned}\alpha_{j_1,j_2\ldots,j_M} = \int_{-\infty}^{+\infty} dQ_1 \int_{-\infty}^{+\infty} dQ_2 \cdots \int_{-\infty}^{+\infty} dQ_M |\psi_{j_1}(Q_1)|^2 \cdot |\psi_{j_2}(Q_2)|^2 \ldots |\psi_{j_M}(Q_M)|^2 \alpha(Q_1, Q_2, \ldots, Q_M) = \\ \langle j_1, j_2, \ldots, j_M|\,\hat{\alpha}\,|j_1, j_2, \ldots, j_M\rangle\end{aligned} \tag{S13}$$

As above, the macroscopic polarizability is obtained as the thermal average

$$\alpha(T) = \sum_{j_1,j_2,\ldots,j_M} p_{j_1} \cdot p_{j_2} \ldots p_{j_M} \alpha_{j_1,j_2\ldots,j_M}$$

Importantly, aiming to focus on a single vibrational degree of freedom (for example, j_1), an effective temperature dependent polarizability $\alpha_{j_1}(T)$, which in principle depends also on j_1, can be defined marginalizing over the other different vibrational degrees of freedom (j_2, …, j_M). Namely,

$$\alpha_{j_1}(T) = \sum_{j_2,\ldots,j_M} p_{j_2} \ldots p_{j_M} \alpha_{j_1,j_2\ldots,j_M}$$

which can be expressed as

$$\alpha_{j_1}(T) = \int_{-\infty}^{+\infty} dQ_1 |\psi_{j_1}(Q_1)|^2 \cdot \sum_{j_2,\dots j_M} p_{j_2} \dots p_{j_M} \int_{-\infty}^{+\infty} dQ_2 \cdots \int_{-\infty}^{+\infty} dQ_M \alpha(Q_1, Q_2, \dots, Q_M) |\psi_{j_2}(Q_2)|^2 \dots |\psi_{j_M}(Q_M)|^2$$

$$\alpha_{j_1}(T) = \int_{-\infty}^{+\infty} dQ_1 |\psi_{j_1}(Q_1)|^2 \cdot \alpha_{\text{eff}}(Q_1, T) \tag{S14}$$

where

$$\alpha_{\text{eff}}(Q_1, T) = \sum_{j_2,\dots j_M} p_{j_2} \dots p_{j_M} \int_{-\infty}^{+\infty} dQ_2 \cdots \int_{-\infty}^{+\infty} dQ_M \alpha(Q_1, Q_2, \dots, Q_M) |\psi_{j_2}(Q_2)|^2 \dots |\psi_{j_M}(Q_M)|^2 \tag{S15}$$

In analogy with the diatomic molecule, the dependence on the occupancy of a single vibrational degree can be in general neglected (i.e., assuming $\alpha_{j_1}(T) = \alpha(T)$), while significant variations of the polarizability can still occur at different temperatures, due to the average over the other (many) degrees of freedom appearing on Eq. S15.

EXPERIMENTAL SETUP

The temperature dependence of both stimulated Raman and spontaneous responses has been measured using a commercial temperature controlled stage (THMS600 by Linkam). Temperature has been monitored via a platinum sensor. Calibration and homogeneous thermal distribution of the sample were verified using a second 10 kΩ thermistor sensor positioned at the opposite end of the sample.

Stimulated Raman A Stimulated Raman scattering (SRS) experiment requires two pulses temporally and spatially overlapped on the sample under investigation [12, 13], namely a narrowband ($\approx 10 - 20$ cm^{-1}) Raman pump (RP), which ensures high spectral resolution, and a femtosecond broadband probe pulse (PP). The RP and the PP used for the SRS experiment have been synthesized from a Ti:sapphire laser source, which generates 40 fs transform limited pulses centered at 800 nm, with an energy of 2.5 mJ and 1 kHz of repetition rate. The PP has been obtained via supercontinuum generation, focusing a small fraction of the laser on a 3-mm-sapphire crystal, producing a broadband (450-1000 nm) white light continuum (WLC). For the synthesis of the RP, a commercial two-stage optical parametric amplifier [14] (Light Conversion TOPAS-C) is used to produce tunable IR-visible pulses, which are then frequency doubled by spectral compression (SC) via second harmonic and sum frequency generation [15, 16] in a 25 mm-thick BBO crystal to produce a beam centered at $\lambda_R \approx 630$ nm. The RP generated by SC are characterized by a temporal envelope unfavorable for SRS, which is rectified by a double-pass (2f) spectral filter, obtaining a Gaussian profile with ≈ 3 ps time duration [17]. The pulses are then focused on the sample in a non-collinear geometry ($\approx 5°$) and the PP spectrum is monitored on a charge-coupled device (CCD) upon frequency dispersion by a spectrometer (Acton Spectra Pro 2500i).

Spontaneous Raman A Spontaneous Raman (SR) experiment requires a narrowband source to be focused on the sample under investigation, collecting and spectrally resolving the inelastically scattered light. To control the output polarization of a 20mW, 473nm continuous wave laser source, a half-wave plate and a Glan-Laser Calcite Polarizer are employed. This laser source is then focused onto the sample through a 15 mm focal length aspherical lens. The back-scattered Raman radiation is collected by the same lens, suppressing the Rayleigh component by a polarizing beam splitter. The emitted Raman spectrum is monitored using a charge-coupled device (CCD) upon frequency dispersion by a spectrometer (Acton Spectra Pro 2500i).

---

[*] giovanni.batignani@uniroma1.it and tullio.scopigno@uniroma1.it

[1] L. Monacelli, G. Batignani, G. Fumero, C. Ferrante, S. Mukamel, and T. Scopigno, Manipulating impulsive stimulated raman spectroscopy with a chirped probe pulse, J. Phys. Chem. Lett. **8**, 966 (2017).

[2] G. Batignani, C. Ferrante, G. Fumero, and T. Scopigno, Broadband impulsive stimulated raman scattering based on a chirped detection, J. Phys. Chem. Lett. **10**, 7789 (2019).

[3] E. Mai, P. Malakar, G. Batignani, M. Martinati, S. Ruhman, and T. Scopigno, Orchestrating nuclear dynamics in a permanganate doped crystal with chirped pump–probe spectroscopy, The Journal of Physical Chemistry Letters **15**, 6634 (2024).

[4] I. Gdor, T. Ghosh, O. Lioubashevski, and S. Ruhman, Nonresonant raman effects on femtosecond pump–probe with chirped white light: Challenges and opportunities, J. Phys. Chem. Lett. **8**, 1920 (2017).
[5] S. Mukamel, Controlling multidimensional off-resonant-raman and infrared vibrational spectroscopy by finite pulse band shapes, The Journal of chemical physics **130**, 054110 (2009).
[6] D. Polli, V. Kumar, C. M. Valensise, M. Marangoni, and G. Cerullo, Broadband coherent raman scattering microscopy, Laser Photonics Rev. **12**, 1800020 (2018).
[7] E. O. Potma and S. Mukamel, Theory of coherent raman scattering, in *Coherent Raman Scattering Microscopy*, edited by J.-X. Cheng and X. S. Xie (CRC Press, Boca Raton, FL, 2012).
[8] A. Virga, C. Ferrante, G. Batignani, D. D. Fazio, A. D. G. Nunn, A. C. Ferrari, G. Cerullo, and T. Scopigno, Coherent anti-stokes raman spectroscopy of single and multi-layer graphene, Nat. Commun. **10**, 10.1038/s41467-019-11165-1 (2019).
[9] J. T. Fourkas, H. Kawashima, and K. A. Nelson, Theory of nonlinear optical experiments with harmonic oscillators, The Journal of Chemical Physics **103**, 4393 (1995).
[10] V. Kemlin, A. Bonvalet, L. Daniault, and M. Joffre, Transient two-dimensional infrared spectroscopy in a vibrational ladder, The Journal of Physical Chemistry Letters **7**, 3377 (2016).
[11] R. P. Bell, Polarisibility and internuclear distance, Transactions of the Faraday Society **38**, 422 (1942).
[12] G. Batignani, C. Ferrante, G. Fumero, M. Martinati, and T. Scopigno, Femtosecond stimulated raman spectroscopy, Nat. Rev. Methods Primers **4**, 10.1038/s43586-024-00314-6 (2024).
[13] G. Batignani, G. Fumero, E. Pontecorvo, C. Ferrante, S. Mukamel, and T. Scopigno, Genuine dynamics vs cross phase modulation artefacts in femtosecond stimulated raman spectroscopy, ACS Photonics **6**, 492 (2019).
[14] C. Manzoni and G. Cerullo, Design criteria for ultrafast optical parametric amplifiers, J. Opt. **18**, 103501 (2016).
[15] M. A. Marangoni, D. Brida, M. Quintavalle, G. Cirmi, F. M. Pigozzo, C. Manzoni, F. Baronio, A. D. Capobianco, and G. Cerullo, Narrow-bandwidth picosecond pulses by spectral compression of femtosecond pulses in second-order nonlinear crystals, Opt. Express **15**, 8884 (2007).
[16] E. Pontecorvo, S. Kapetanaki, M. Badioli, D. Brida, M. Marangoni, G. Cerullo, and T. Scopigno, Femtosecond stimulated raman spectrometer in the 320-520nm range, Opt. Express **19**, 1107 (2011).
[17] E. Pontecorvo, C. Ferrante, C. G. Elles, and T. Scopigno, Spectrally tailored narrowband pulses for femtosecond stimulated raman spectroscopy in the range 330-750 nm, Opt. Express **21**, 6866 (2013).